Hindawi Publishing Corporation
International Journal of Antennas and Propagation
Volume 2008, Article ID 456019, 10 pages
doi:10.1155/2008/456019

Research Article

An Antenna-Theory Method for Modeling High-Frequency RF Coils: A Segmented Birdcage Example

Xin Chen,[1] Victor Taracila,[2] Timothy Eagan,[3] Hiroyuki Fujita,[1,4,5] Xingxian Shou,[1] Tanvir Baig,[6] and Robert Brown[1]

[1] *Department of Physics, Case Western Reserve University, 10900 Euclid Avenue, Cleveland, OH 44106, USA*
[2] *GE Healthcare, Aurora, OH 44202, USA*
[3] *Philips Medical Systems, Highland Heights, OH 44143, USA*
[4] *Department of Radiology, University Hospitals of Cleveland, Cleveland, OH 44106, USA*
[5] *Quality Electrodynamics LLC, Mayfield Village, OH 44143-2336, USA*
[6] *Department of Physics, University of Dhaka, Dhaka 1000, Bangladesh*

Correspondence should be addressed to Robert Brown, rwb@case.edu

Received 2 August 2007; Revised 4 December 2007; Accepted 12 February 2008

Recommended by Stuart Crozier

We suggest that center-fed dipole antenna analytics can be employed in the optimized design of high-frequency MRI RF coil applications. The method is illustrated in the design of a single-segmented birdcage model and a short multisegmented birdcage model. As a byproduct, it is shown that for a long single-segmented birdcage model, the RF field within it is essentially a TEM mode and has excellent planar uniformity. For a short shielded multisegmented birdcage model, the RF field is optimized with a target-field approach with an average SAR functional. The planar homogeneity of the optimized RF field is significantly improved compared with that of a single-segmented birdcage model with the same geometry. The accuracy of the antenna formulae is also verified with numerical simulations performed via commercial software. The model discussed herein provides evidence for the effectiveness of antenna methods in future RF coil analysis.

1. INTRODUCTION

Radiofrequency (RF) field inhomogeneity has been a major challenge in today's high-field magnetic resonance imaging (MRI) mainly due to the shortened RF wavelength in human tissue at higher frequencies. It has been shown [1] that image quality can be significantly affected. Recently, both experimental and theoretical work have been presented to improve the RF field homogeneity, such as the *TEM resonator* [2, 3], closed-form analytical solutions [4–8], and numerical simulations [9–11]. Techniques such as RF shimming [11] and parallel transmission [12] are applied to improve the RF field homogeneity with a focus on the transmit coil array. Although theoretical progress has been made in analyzing the experimental results, and RF field homogeneity can be improved with various techniques, a better understanding of the relationship between the RF current sources and the RF fields is still needed. A modeling control of the source-field relationship can be used to optimize the RF performance, much as has been done, for instance, in [13], for lower frequencies. Moreover, the specific absorption rate (SAR) is an important RF safety concern as more RF energy tends to be deposited into human tissue in high-field MRI experiments [14]. Although detailed numerical simulations have been presented to analyze the SAR distribution in the human head within volume and surface coils [15, 16], there is an absence of RF coil models that incorporate both RF field and SAR calculation and optimization. In this paper, we show that analytic formulae found in antenna theory can be applied with success in the optimized design of RF coils. It is well known that a static surface current distribution which is sinusoidal in the azimuthal direction on a surface of a cylinder produces a homogeneous static magnetic field everywhere in the cylinder [17]. We find that in a high frequency case, such sinusoidal current distribution can produce magnetic field which is uniform in transverse planes and oscillates in the direction perpendicular to the transverse plane; thus transverse electromagnetic (TEM) mode can be

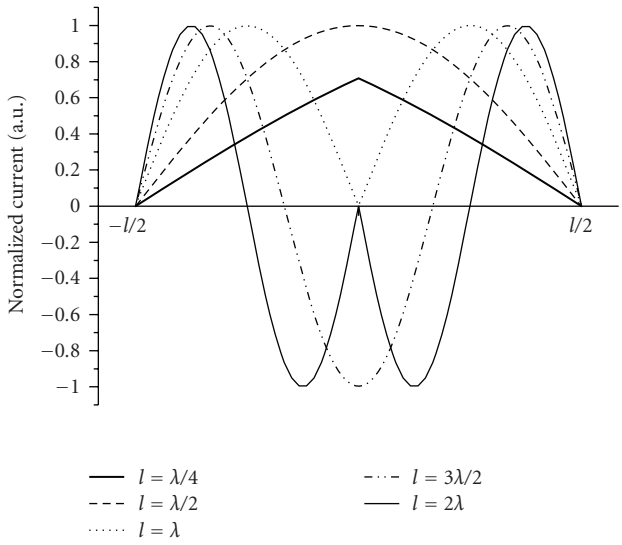

Figure 1: Current distribution on a center-fed dipole antenna for different antenna's lengths. λ is the wavelength of the oscillating current source.

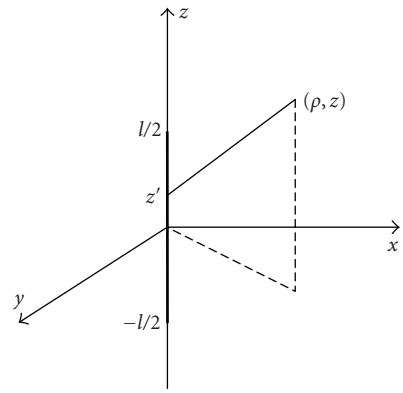

Figure 2: Schematic of an idealized center-fed dipole antenna with length l.

supported. With our model we show that by restricting the oscillation of the field required by Maxwell equations to the longitudinal direction, homogeneity in transverse planes can be significantly improved, as demonstrated in [5].

2. METHODS

A good approximation of the oscillating current on a center-fed dipole antenna is a sinusoidal standing wave current with nodes at both ends [18] (Figure 1):

$$\mathbf{I}(x'=0,y'=0,z') = \begin{cases} \mathbf{e}_z I_0 \sin\left[k\left(\frac{l}{2}-z'\right)\right], & 0 \le z' \le \frac{l}{2}, \\ \mathbf{e}_z I_0 \sin\left[k\left(\frac{l}{2}+z'\right)\right], & -\frac{l}{2} \le z' \le 0. \end{cases} \tag{1}$$

Here I_0 is the current amplitude, k is the wave number (i.e., 2π/wavelength), and l is the length of the antenna. It is assumed that the antenna has negligible cross section and is aligned along the z direction with its center at the origin, as shown in Figure 2. The vector potential and the magnetic field produced by this center-fed dipole antenna are therefore determined [18]:

$$\mathbf{A}(\rho,z) = \frac{\mu_0}{4\pi}\int_{-l/2}^{l/2} \mathbf{I}(z')\frac{e^{-ik\sqrt{\rho^2+(z-z')^2}}}{\sqrt{\rho^2+(z-z')^2}}dz', \tag{2}$$

$$\begin{aligned}\mathbf{B}(\rho,z) &= \nabla\times\mathbf{A}(\rho,z) \\ &= -\frac{\mu_0 I_0}{4\pi i}\frac{1}{\rho}\Bigg[e^{-ik\sqrt{\rho^2+(z-l/2)^2}} + e^{-ik\sqrt{\rho^2+(z+l/2)^2}} \\ &\qquad - 2\cos\left(\frac{kl}{2}\right)e^{-ik\sqrt{\rho^2+z^2}}\Bigg]\mathbf{e}_\varphi.\end{aligned} \tag{3}$$

In (2) and (3), the current distribution is given in (1), (ρ,z) represents the cylindrical coordinates of the observation point in space, and z' determines the location of the source point on the antenna. Given a sinusoidal standing wave current distribution in (1), the magnetic field produced by this source can be calculated analytically at any point in the space with (3).

To model the shorter wavelength effects over relevant dimensions and the average dielectric properties of human head under an RF frequency of 400 MHz, we assume a conducting dielectric with constant permittivity 49.75 and conductivity 0.59 S/m [19] fills up all of space. Therefore, the wavelength for an RF field with frequency 400 MHz (corresponding to 9.4T main magnetic field in proton MRI) is approximately 10.6 cm. We choose this frequency in our modeling as a representative value of interest in today's very high-field MRI research. With the presence of a conducting dielectric and $e^{i\omega t}$ time dependence, the wave number k of the propagation in the dielectric will be complex and satisfy

$$k^2 = \omega^2\mu_0\varepsilon\varepsilon_0 - i\omega\mu_0\sigma. \tag{4}$$

Although the magnetic field (3) is derived from a sinusoidal current distribution with a real wave number k, we will still use (3) with all the wave numbers k replaced by the complex value given in (4) as an approximate representation of the RF field in the conducting dielectric. With the presence of the conductivity, Maxwell equation gives

$$\nabla\times\mathbf{B} = \mu_0\varepsilon\varepsilon_0\frac{\partial\mathbf{E}}{\partial t} + \mu_0\sigma\mathbf{E} = \left(i\omega\mu_0\varepsilon\varepsilon_0 + \mu_0\sigma\right)\mathbf{E}. \tag{5}$$

The electric field can then be determined as

$$\mathbf{E} = \frac{1}{i\omega\mu_0\varepsilon\varepsilon_0 + \mu_0\sigma}\nabla\times\mathbf{B}. \tag{6}$$

Once the electric field is known, the local SAR at a spatial point $\mathbf{r}$ can be estimated as

$$\mathrm{SAR}(\mathbf{r}) = \frac{\sigma}{2\rho}\left|\mathbf{E}(\mathbf{r})\right|^2, \tag{7}$$

and the average SAR in a region of interest is

$$\overline{\mathrm{SAR}} = \frac{1}{N}\sum_{i=1}^{N}\mathrm{SAR}(\mathbf{r}_i), \tag{8}$$

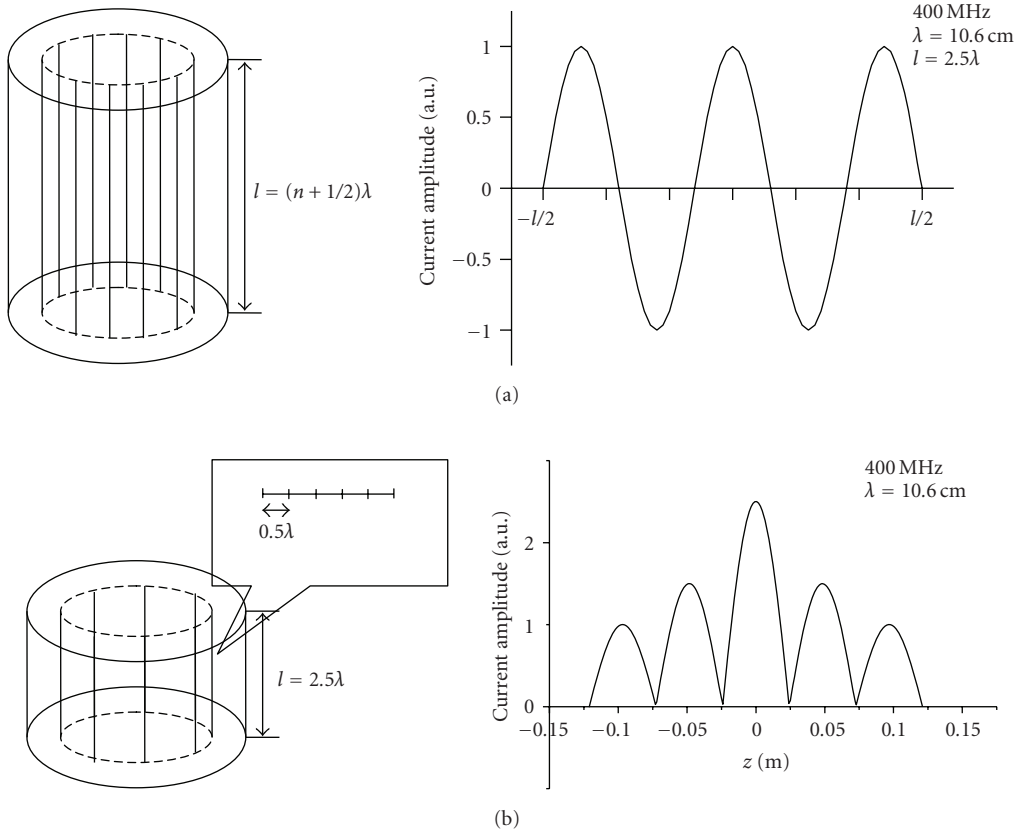

FIGURE 3: (a) Schematics of a shielded single-segmented birdcage model and a representative current distribution on an axial conductor. A model with 10 conductors is shown. The length l satisfies $l = (n + 1/2)\lambda$ where n is an even integer and λ is the wavelength of the source current. A representative current distribution on a 2.5λ-long center-fed dipole antenna is also shown. (b) Schematics of a shielded multisegmented birdcage model and a representative current distribution on an axial conductor consisting with five half-wavelength-long center-fed dipole antennas.

where the density of the dielectric ρ is $1030\,\text{kg/m}^3$ [19] representing an average human head value and $\mathbf{r}_i$ $(i = 1, 2, 3, \ldots, N)$ are N spatial points specified in a region of interest.

A shielded single-segmented birdcage model and a new shielded multisegmented birdcage model are constructed with center-fed dipole antennas as building blocks respectively. The RF fields produced by the two models are separately calculated and compared, after the multisegmented model is optimized with respect to the axial field uniformity and the average SAR. The shielded single-segmented birdcage model (Figure 3(a)) has 16 evenly spaced axial conductors forming a birdcage structure (a model with 10 legs is shown in the picture for clarity) and a cylindrical shield. The inner diameter is 25 cm and the outer diameter is 29 cm, attempting to model a typical head RF coil. Each axial conductor is constructed as a center-fed dipole antenna and there are no end rings. The azimuthal current distribution among conductors is sinusoidal. Along the longitudinal (z) direction, the current has a simple sinusoidal standing wave z-profile as given in (1). It is noted that when the length of the center-fed dipole antenna satisfies $l = (n + 1/2)\lambda$ (where λ is the wavelength of the oscillating current source and n is any even integer), the current distribution (1) becomes $\cos(kz)$. Thus, in order to avoid more complicated charge and current distributions, the length of the center-fed dipole antenna is always assumed to be $(n + 1/2)\lambda$ with n an even integer. Also, to focus on the wavelength effect due to the shortened electromagnetic wavelength by itself we neglect, for the moment, the conductivity of the dielectric for all the calculations related to the RF field distribution of the single-segmented birdcage model. The effect of the shield can be simulated with the image method [20], which states that the field produced by the currents induced on a shield is identical to the field produced by the image of the original current with respect to the shield. In the case of a cylindrical shield, the image of the current flowing in the axial conductor is a current flowing with opposite direction and located coaxially at a distance $R_{\text{sh}}(R_{\text{sh}} - R_0)/R_0$ from the shield, where R_{sh} and R_0 are the outer and inner radii of the birdcage model, respectively. The RF fields of the shielded birdcage model are then determined with (3).

For the shielded multisegmented birdcage model (Figure 3(b)), the length is chosen to be 2.5λ (approximately 26.6 cm). The inner and the outer diameters of the model are 25 cm and 29 cm, respectively, the same as the single-segmented birdcage. There are eight axial conductors and no end rings. Each axial conductor consists of five

half-wavelength-long center-fed dipole antennas. Three of them (the middle segment and the two on one side of the middle segment) are independently fed and the other two on the other side have current sources that are fixed by the axial symmetry around the central transverse plane. The image method described above is also applied here to incorporate the effect of the cylindrical shielding. Based on (3) and (6), the magnetic and the electric fields produced by each RF element (the half-wavelength-long center-fed dipole antenna) can be calculated. Therefore, the magnetic and the electric fields of the model are the superposition of the fields produced by all the individual RF elements and are functions of current amplitudes and phases on these elements. In order to obtain a uniform RF field profile with control over average SAR, a functional is constructed as

$$\begin{aligned} W &= \overline{\mathrm{SAR}} \\ &\quad + \sum_{j=1}^{Nr} \lambda_j \left[B_{1,x}(I_1, \phi_1, I_2, \phi_2, \ldots, I_{N_0}, \phi_{N_0}; \mathbf{r}_j) - B_x^{(\mathrm{target})}(\mathbf{r}_j) \right] \\ &\quad + \sum_{j=1}^{Nr} \mu_j \left[B_{1,y}(I_1, \phi_1, I_2, \phi_2, \ldots, I_{N_0}, \phi_{N_0}; \mathbf{r}_j) - B_y^{(\mathrm{target})}(\mathbf{r}_j) \right] \\ &= \frac{1}{N_{\mathrm{SAR}}} \sum_{i=1}^{N_{\mathrm{SAR}}} \frac{\sigma}{2\rho} \left| \mathbf{E}(\mathbf{r}_i) \right|^2 \\ &\quad + \sum_{j=1}^{Nr} \lambda_j \left[B_{1,x}(I_1, \phi_1, I_2, \phi_2, \ldots, I_{N_0}, \phi_{N_0}; \mathbf{r}_j) - B_x^{(\mathrm{target})}(\mathbf{r}_j) \right] \\ &\quad + \sum_{j=1}^{Nr} \mu_j \left[B_{1,y}(I_1, \phi_1, I_2, \phi_2, \ldots, I_{N_0}, \phi_{N_0}; \mathbf{r}_j) - B_y^{(\mathrm{target})}(\mathbf{r}_j) \right]. \end{aligned} \tag{9}$$

Here, I_i and ϕ_i are the unknown current amplitude and phase on the ith half-wavelength-long center-fed dipole antenna, N_0 is the total number of the antennas (which is equal to 40 in the present model), $\mathbf{r}_j$ is the jth of the N_r total constraint points in the central axial plane where we calculate the x and y components of the RF field produced by the model ($B_{1,x}$ and $B_{1,y}$) and impose the desired target field with both uniform amplitude and phase ($B_x^{(\mathrm{target})} = 0$ and $B_y^{(\mathrm{target})} =$ constant), and $\mathbf{r}_i$ is the ith of the N_{SAR} total spatial points in a region of interest (ROI) where we determine the electric field $\mathbf{E}(\mathbf{r}_i)$ and the local SAR. A cylindrical ROI with a diameter of 16 cm and a length of 8 cm coaxially located within the multisegmented birdcage model, with their centers coincide, is selected for an illustrative SAR calculation. λ_j and μ_j are the familiar Lagrange multipliers. The functional W is minimized to obtain a uniform RF field using a functional approach to control SAR. The minimization is achieved by differentiating with respect to I_i, ϕ_i, λ_j, and μ_j, and solving the obtained $2N_0 + 2N_r$ equations to find $2N_0 + 2N_r$ unknowns I_i, ϕ_i, λ_j, and μ_j. Since the SAR term is a quadratic function of unknown current amplitudes and phases, the $2N_0 + 2N_r$ equations are all linear and can be solved with matrix inversion. Optimal current amplitudes and phases are found and can be employed as sources parameters to determine the corresponding RF field and SAR profiles.

3. RESULTS

The single-segmented birdcage model is assumed to be driven by a current that is sinusoidal in the azimuthal direction around any transverse plane

$$I_j = I_0 e^{i(\omega t + \phi_j)}, \tag{10}$$

where I_j and ϕ_j are the current amplitude and phase in the jth axial conductor, and the phase ϕ_j coincides with the azimuthal angle of the axial conductor. The RF fields produced by models with different lengths $l = (n + 1/2)\lambda$ are calculated with the analytical formula (3). It is shown that with fixed diameter, the longer model has increasingly better RF field uniformity. Figure 4 shows maps of the amplitude of the clockwise component of the circularly polarized RF field (the component contributing to the excitation of the nucleus spins) in the central transverse plane for single-segmented birdcage models with lengths (a) 2.5λ (approximately 26.6 cm), (b) 10.5λ (approximately 1.12 m), (c) 20.5λ (approximately 2.18 m), and (d) 100.5λ (approximately 10.7 m). The normalized RF field amplitude across the central transverse plane along the x-axis is also shown (Figure 4(e)). In terms of the maximum percentage deviation from the field at the center, the model with a length of 2.5λ has a nonuniformity of 60%, the one with a length of 10.5λ has a value of 32%, the 20.5λ-long model has a value of 10%, and the 100.5λ-long model only has a nonuniformity of 0.4%. The normalized amplitude of the RF field along the longitudinal direction (z direction) is shown in Figure 5. As the length of the model increases, the oscillation of the field in the z direction approaches the absolute value of $\cos(kz)$, where k is the wave number of propagation in the dielectric. In contrast to a low-frequency birdcage, the length of the coil has to be very long before excellent transverse uniformity is achieved.

The unknown current amplitudes and phases of a multisegmented birdcage model are found through the aforementioned optimization process. Table 1 shows current amplitudes and phases among the eight half-wavelength-long center-fed dipole antennas of three independent-fed sections (i.e., the middle section, the section to the right (left) of the middle section, and the rightmost (leftmost) section) for the B1 field strength 1.16 μT at the center of the model. The symmetry of the current amplitudes implies that among the eight antenna segments of any section only four of them are independent. The current phases, nev-ertheless, do not exhibit any specific symmetries or relations with the azimuthal angles of the RF elements. The RF field optimized for uniformity in the central transverse plane is calculated with the solved currents. Figure 6 shows the map of the amplitude of the clockwise component of the circularly polarized RF field and the variation of the field along the x-axis in the central transverse plane of the optimized multisegmented birdcage model. It can bee seen that in the central region, the RF field variation is below 20%, compared with a nearly 60% variation of a single-segmented birdcage model (Figure 4). Figure 7 shows the RF field variation along the longitudinal (z) direction for the optimized multisegmented birdcage. The field pattern

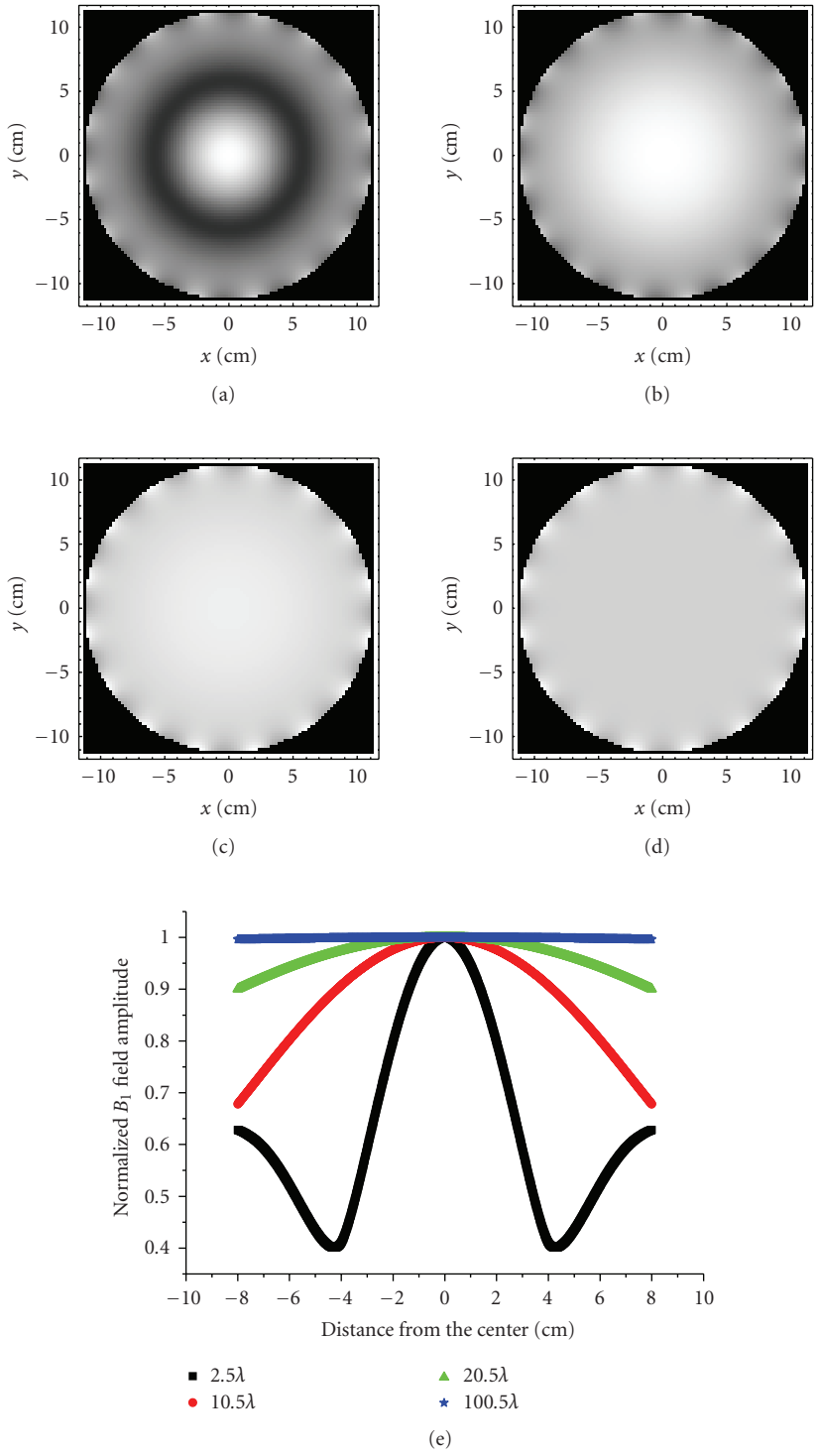

FIGURE 4: Amplitude of the clockwise component of the circularly polarized RF field in the central transverse planes for the single-segmented birdcage models with length (a) 2.5λ, (b) 10.5λ, (c) 20.5λ, and (d) 100.5λ. In (e), the normalized field variation across the central transverse plane along x-axis is shown.

coincides with the absolute value of $\cos(\alpha z)$ in the proximity of $z = 0$, where α is the real part of the complex wave number of the propagation in the dielectric. The average SAR within the aforementioned cylindrical ROI of this optimized model is 3.7 W/kg.

4. DISCUSSION

Due to the shortened RF field wavelength inside human tissue for high-field MRI, it is more difficult to use conventional RF coils to generate uniform RF field over the imaging

Table 1: Optimal current (a) amplitudes and (b) phases of the half-wavelength-long center-fed dipole antenna elements in the multisegmented birdcage model.

(a) Current amplitudes/A

Azimuthal angle of RF elements/degree	22.5	67.5	112.5	157.5	202.5	247.5	292.5	337.5
The rightmost (leftmost) section	10.95	7.45	3.47	12.38	10.95	7.45	3.47	12.38
The right (left) section	6.35	4.23	2.65	7.43	6.35	4.23	2.65	7.43
The middle section	4.02	2.88	2.26	5.32	4.02	2.88	2.26	5.32

(b) Current phases/degree

Azimuthal angle of RF elements/degree	22.5	67.5	112.5	157.5	202.5	247.5	292.5	337.5
The rightmost (leftmost) section	158.59	216.59	264.86	317.69	338.59	36.59	84.86	137.69
The right (left) section	283.06	335.27	23.05	90.43	103.06	155.27	203.05	270.43
The middle section	95.49	145.82	196.06	268.50	275.49	325.82	16.06	88.5005

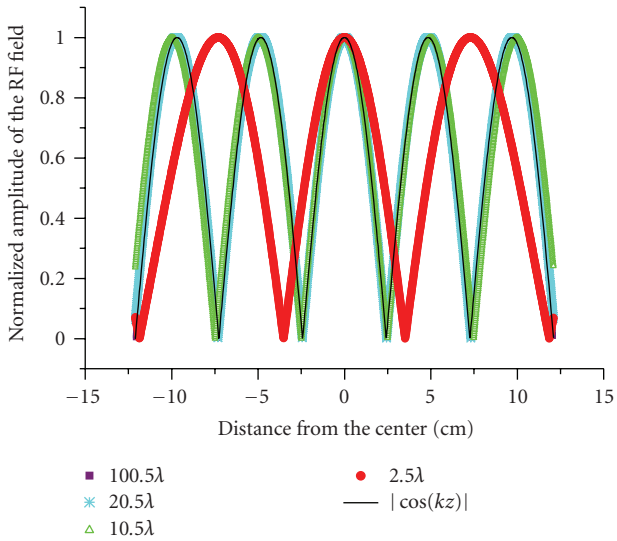

Figure 5: RF field variation along the longitudinal (z) direction for single-segmented birdcage models with different lengths. The results are all compared with the absolute value of the cosine function.

region of interest. In terms of theoretical considerations, the Biot-Savart law, which is widely applied to determine the RF field in the low-frequency regime, is unable to give accurate predictions for the RF field of high frequency. For high-field MRI, most of the theoretical calculations and simulations are performed with commercial software and iterative numerical algorithms. Whatever analytical solutions that have been found previously available are mathematically complicated and have rarely been used to simulate modern RF applications, such as RF shimming and parallel transmission. In this paper, we have applied new analytic formulae from antenna theory to calculate the RF fields for a representative class of RF coils, namely, head coils with a birdcage structure. For the single-segmented birdcage model (with single center-fed dipole antennas used for each axial conductor), at high frequency, increasing the length leads to improved central planar uniformity for the RF field. In fact, if the length of the model is much larger than the fixed diameter, the oscillation of the RF field required by Maxwell equations will be restricted to the longitudinal direction and excellent uniformity of the RF field in any of the transverse slices can be achieved. (In the limit of infinite length, the uniformity is perfect.)

In the long-coil limit, the electromagnetic fields inside approach a TEM mode. In this limit, the current and charge distributions on the coils have the same sinusoidal azimuthal dependence, $\sin\varphi$ as found for the low-frequency birdcage, both yielding internal magnetic fields that are spatially uniform and pointing along the x-axis. Let us see how this sinusoidal azimuthal dependence arises from waveguide theory, where it is well known [17] that, for a TEM wave, Maxwell equations become

$$\nabla_t^2 \begin{Bmatrix} \mathbf{E} \\ \mathbf{B} \end{Bmatrix} = \left(\nabla^2 - \frac{\partial^2}{\partial z^2}\right) \begin{Bmatrix} \mathbf{E} \\ \mathbf{B} \end{Bmatrix} = 0. \tag{11}$$

This means that the electric field is a solution of a two-dimensional electrostatic-like problem in the transverse plane perpendicular to the wave propagation direction. Although the TEM mode cannot exist inside a single hollow (good) conductor, which generates an equipotential surface, it can be supported with two or more conductor surfaces such as a coaxial cable or transmission line, or a surface around which the potential is not constrained to be constant. Suppose a cylinder is formed by such surfaces, and a TEM electromagnetic wave (which can be either a standing wave or a traveling wave) exists in this cylinder such that the electric and magnetic fields in any transverse plane are uniform. For example, suppose a spatially uniform magnetic field points along the x-axis and a spatially uniform electric field points along the y-axis. At the surfaces, the electric and magnetic fields must satisfy the familiar boundary discontinuity conditions

$$\begin{aligned} (\mathbf{E}_{\text{out}} - \mathbf{E}_{\text{in}}) \cdot \mathbf{n} &= \frac{\sigma}{\varepsilon_0}, \\ \mathbf{n} \times (\mathbf{B}_{\text{out}} - \mathbf{B}_{\text{in}}) &= \mu_0 \mathbf{K}, \end{aligned} \tag{12}$$

where $\mathbf{E}_{\text{in}}$ and $\mathbf{E}_{\text{out}}$ ($\mathbf{B}_{\text{in}}$ and $\mathbf{B}_{\text{out}}$)represent the electric (magnetic) fields inside and outside the surface, respectively,

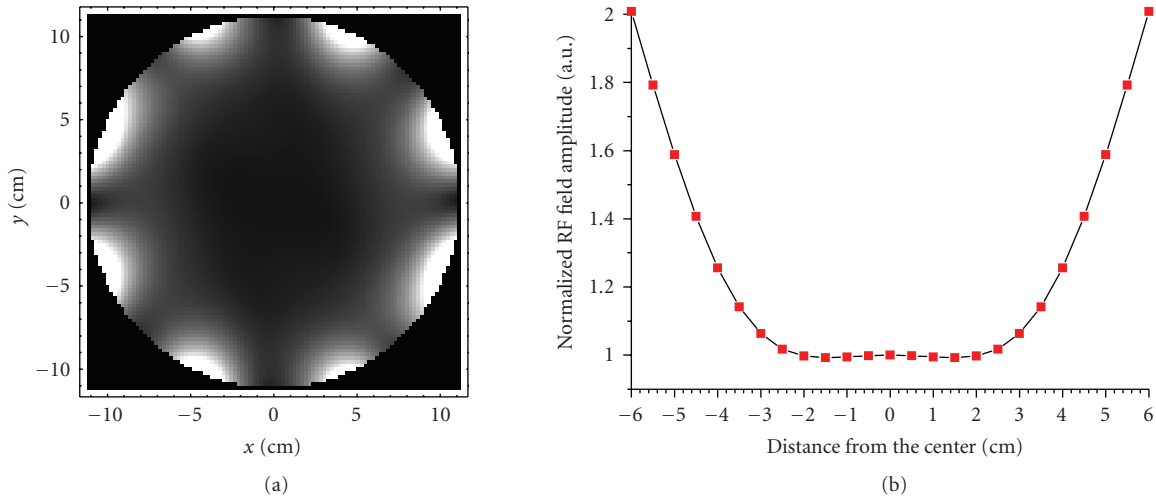

Figure 6: Amplitude of the RF field in the central axial plane (a) and across the diameter along the horizontal (x) direction (b) for the optimized multisegmented birdcage model.

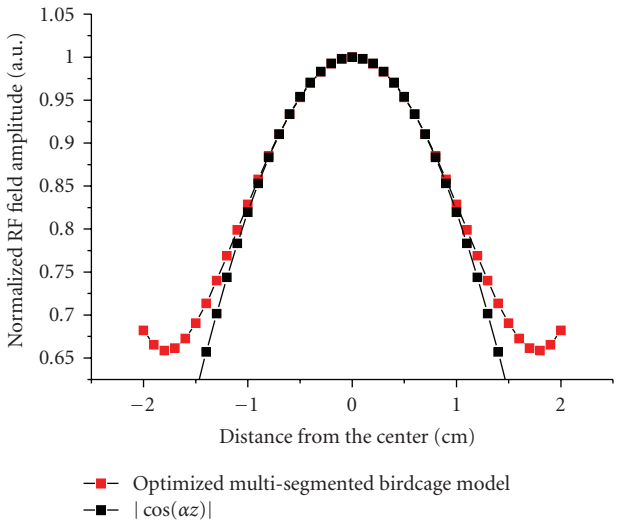

Figure 7: RF field variation along the longitudinal (z) direction of the optimized multisegmented birdcage model.

$\sigma(\mathbf{K})$ is the surface electric charge (current) density, and the normal (to the surface) vector $\mathbf{n}$ points from the inside of the cylinder toward the outside of the cylinder. In the case where the electric and the magnetic fields outside the coil are zero, and the electric (magnetic) field is uniform inside the cylinder and along the y-axis (x-axis), we have

$$\begin{aligned}(0 - E_0\mathbf{e}_y)\cdot(\cos\varphi\mathbf{e}_x + \sin\varphi\mathbf{e}_y) &= \frac{\sigma}{\varepsilon_0},\\ (\cos\varphi\mathbf{e}_x + \sin\varphi\mathbf{e}_y)\times(0 - B_0\mathbf{e}_x) &= \mu_0\mathbf{K},\end{aligned} \tag{13}$$

where E_0 (B_0) is the magnitude of the spatially uniform electric (magnetic) field, $\mathbf{e}_x$ and $\mathbf{e}_y$ are unit vectors pointing, respectively, along the x and y directions, and φ is the azimuthal angle. It can be seen that the azimuthal distribution of the electric charge and the surface current density are both proportional to $\sin\varphi$ where φ is the azimuthal angle, and the direction of the current flow points along the z direction. These results are consistent with our calculations.

Although an infinitely long birdcage model with conventional sinusoidal current distribution can support a perfectly uniform TEM mode, a short one with length comparable to a normal RF head coil can not. Therefore, we have constructed a multisegmented birdcage model with a large number of center-fed dipole antenna RF elements. Each of the original axial conductors in the single-segmented birdcage model is now replaced by five equal subleg segments in our example. With our analytical tools the RF field can be calculated and optimized. The optimal RF field shows excellent central planar uniformity. In other words, a kind of RF shimming is achievable with our model and theory. Although excellent RF field planar homogeneity is achieved with our optimization process in the central transverse plane, the RF field uniformity degrades rapidly as the transverse plane moves away from the center of the model. It can be seen in Figure 7 that the oscillation of the field coincides with the absolute value of the cosine function only around $z = 0$. It implies that perfect sinusoidal longitudinal (along z) oscillation of the field is approximately restricted to the $z = 0$ region, and, as a result, the (transverse) field within the central transverse plane is approximately uniform. Although in the present solution the planar uniformity of the RF field degrades rapidly as the transverse plane moves away from the center, a similar optimization can be performed over other transverse planes to improve the field uniformity. Although the planar RF field homogeneity is improved, it is noted that the field strength significantly increases toward the periphery of the central axial plane. This is due to large current amplitudes in the antenna RF elements (Table 1). In fact, in our present solution, the uniform field in the central transverse plane is a result of partial cancellations among the fields produced by individual antenna elements. Therefore, the current amplitudes on the

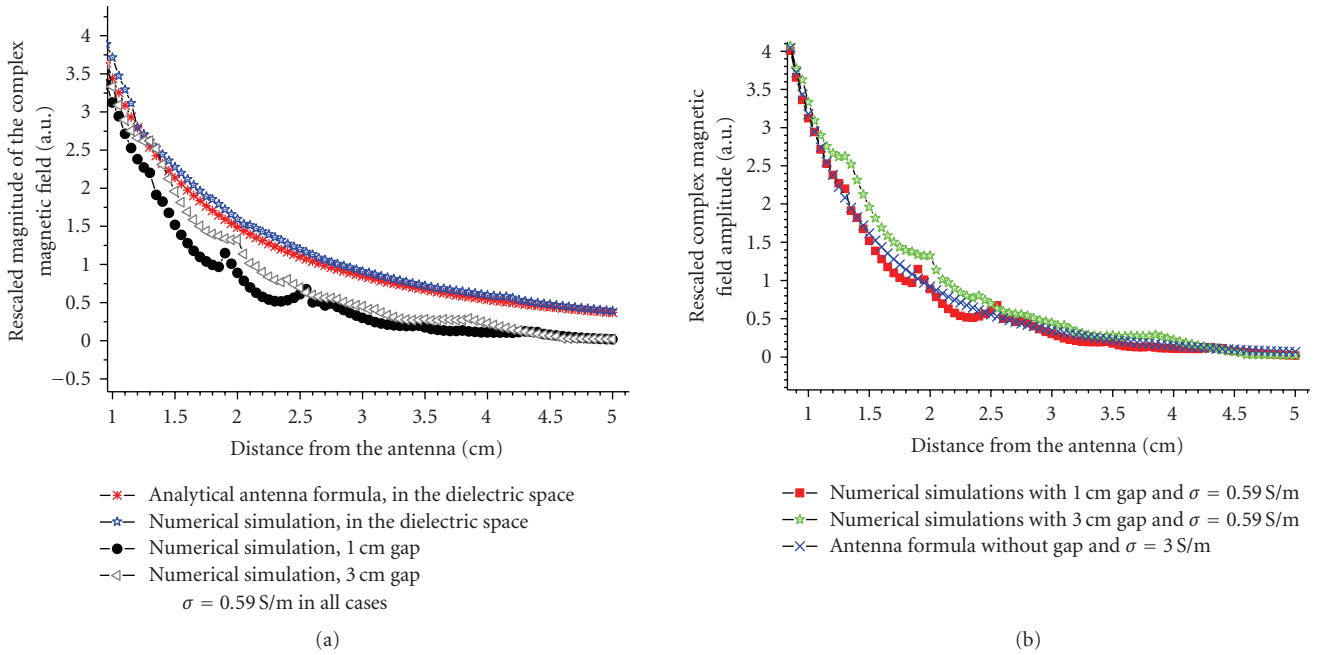

Figure 8: Complex magnetic field amplitude calculated with the analytic antenna formula and with the numerical simulation under different conditions. The field strength is rescaled for comparison.

antenna elements tend to increase to produce a reasonable RF field strength in the central region of the axial plane. The increased currents lead to stronger both magnetic and electric fields at the periphery. As a result, the average SAR is bigger than results presented in some other numerical simulations such as [21]. It is difficult to reduce the SAR under the constraints demanding uniform RF field. In order to address this problem, we may perform the optimization process in a smaller region of interest to balance the RF field homogeneity and the SAR. In our present model, we have assumed a current distribution that oscillates with a dielectric wavelength to make an analytic solution possible. In fact, with the more general endpoints for our sinusoidal current z-profile formula, by superposition treating different kinds of the current z-profiles, we can approximate, for example, a more uniform current z-profile.

In our modeling, we have assumed that the dielectric fills up the whole of space instead of assuming a layer of air between the coil and a cylindrical dielectric phantom [5–8] or using a heterogeneous head model [9–11]. We make this approximation mainly for simplifying our analytic calculations. To estimate the error of this approximation, we performed numerical simulations with HFSS (Ansoft Corporation) to study the RF field produced by our building blocks (half-wave-length-long center-fed dipole antennas) under several different conditions. Figure 8(a) shows the amplitude of the complex magnetic field at $z = 0$ as a function of the radial distance from a half-wavelength-long center-fed dipole antenna aligned along the z-axis with its center at the origin (as shown in Figure 2). The fields are rescaled such that they are identical 0.8 cm away from the antenna. Fields under the following conditions are plotted: (i) fields calculated with our analytic antenna formula with a dielectric filling up the whole space, (ii) fields calculated with numerical simulations with a dielectric filling up the whole space, (iii) the antenna is located coaxially 12.5 cm from the central axis of a dielectric cylinder with radius 11.5 cm (i.e., there is a 1 cm air gap between the antenna and the surface of the cylinder), and (iv) the antenna is located coaxially 12.5 cm from the central axis of a dielectric cylinder with radius 9.5 cm (i.e., there is a 3 cm air gap between the antenna and the surface of the cylinder). It is shown that with the dielectric properties of an average human head, there is an excellent agreement between the analytic antenna formula and the numerical simulations without the presence of any air gap. The error introduced by the approximation that ignores the air gaps is an overall scaling difference of the field strength as long as the field is not estimated close to the antenna (typically, at least 2 cm away from the antenna). The very interesting point is that, by adjusting the conductivity to 3 S/m, the antenna formula and the "dielectric space" assumption can provide an excellent fit to the field distribution obtained with numerical simulation where there is an air gap between the antenna and the dielectric cylinder, as shown in Figure 8(b). These results suggest that the analytic antenna formulae are useful for modeling practical RF coils. Although further calculations can be performed to address the problem with different layers of dielectric, our present results illustrate how RF field inhomogeneity is caused by the so-called wavelength effect and the manner in which we can achieve a desired RF field pattern through RF shimming. In a more realistic, heterogeneous case, improved RF field homogeneity can be anticipated using the present antenna solution as input

followed by numerical algorithms in an iteration procedure, in order to converge to a better approximation.

Finally, the question arises about the construction of an RF coil based on our model and theory. Although our present model has a total number of 40 antenna RF elements, these elements are not independent. First of all, the aforementioned symmetry with respect to the central axial plane of the multisegmented birdcage model reduces the number of independent current sources from $5 \times 8 = 40$ to $3 \times 8 = 24$. Furthermore, the current amplitudes found with the optimization (as shown in Table 1) have certain symmetry such that the current amplitude of one antenna element is always identical to the current amplitude of the antenna element diagonal to it. Although current phases do not exhibit any specific symmetry, the optimal solution may lead to further reduction of independent current sources. While the purpose of the present work is to present a theoretical tool for an initial optimization, there are multiple solutions to the practical problems. For example, with respect to decoupling in transmit mode, we could start with overlapping the nearest neighbor coils and then add combinations of capacitive or inductive elements for the decoupling of the remaining (next nearest neighbor and beyond) interactions. In particular, the present multisegmented birdcage model, in any case, can be implemented as a "parallel transmit volume coil with independent control of currents on the array elements" [22]. The techniques presented in [22] can be applied to address the problems of decoupling and feeding for constructing a practical coil based on the present model.

5. CONCLUSION

Due to the shortened wavelength of the RF field, RF field inhomogeneity has become a major challenge for high-field MRI. We present an analytic tool to simulate the RF field in the appropriate high-frequency limit. It is shown that an analytic calculation based on antenna theory and an optimization on that modeling can be effectively carried out. RF shimming is achievable to produce RF field with excellent planar uniformity. Our model and analytical calculations can help understand the relationship between the current sources and the RF fields. The major advantage of the present analytic tools is efficiency; for instance, the calculations are much faster than numerical iterative algorithms (by orders of magnitude in comparisons with field calculations performed through numerical integrations). Important parameters such as SAR can also be incorporated into the calculation and optimization. We believe that the methods described here will be quite useful in future RF coil designs.

ACKNOWLEDGMENTS

The authors are grateful to Shmaryu Shvartsman for helpful discussions. They would like to thank Mark Griswold and Jeremy Heilman for discussing practical coil designs based on The authors model. This work is supported by the State of Ohio Third Frontier initiative.

REFERENCES

[1] J. T. Vaughan, M. Garwood, C. M. Collins, et al., "7T vs. 4T: RF power, homogeneity, and signal-to-noise comparison in head images," *Magnetic Resonance in Medicine*, vol. 46, no. 1, pp. 24–30, 2001.

[2] J. T. Vaughan, H. P. Hetherington, J. O. Otu, J. W. Pan, and G. M. Pohost, "High frequency volume coils for clinical NMR imaging and spectroscopy," *Magnetic Resonance in Medicine*, vol. 32, no. 2, pp. 206–218, 1994.

[3] J. T. Vaughan, G. Adriany, C. J. Snyder, et al., "Efficient high-frequency body coil for high-field MRI," *Magnetic Resonance in Medicine*, vol. 52, no. 4, pp. 851–859, 2004.

[4] J. Tropp, "Image brightening in samples of high dielectric constant," *Journal of Magnetic Resonance*, vol. 167, no. 1, pp. 12–24, 2004.

[5] T. K. F. Foo, C. E. Hayes, and Y.-W. Kang, "Reduction of RF penetration effects in high field imaging," *Magnetic Resonance in Medicine*, vol. 23, no. 2, pp. 287–301, 1992.

[6] T. K. F. Foo, C. E. Hayes, and Y.-W. Kang, "An analytical model for the design of RF resonators for MR body imaging," *Magnetic Resonance in Medicine*, vol. 21, no. 2, pp. 165–177, 1991.

[7] D. K. Spence and S. M. Wright, "2-D full wave solution for the analysis and design of birdcage coils," *Concepts in Magnetic Resonance Part B*, vol. 18B, no. 1, pp. 15–23, 2003.

[8] V. Taracila, L. S. Petropoulos, T. P. Eagan, and R. W. Brown, "Image uniformity improvement for birdcage-like volume coils at 400 MHz using multichannel excitations," *Concepts in Magnetic Resonance Part B*, vol. 29B, no. 3, pp. 153–160, 2006.

[9] T. S. Ibrahim, R. Lee, B. A. Baertlein, A. M. Abduljalil, H. Zhua, and P.-M. L. Robitaille, "Effect of RF coil excitation on field inhomogeneity at ultra high fields: a field optimized TEM resonator," *Magnetic Resonance Imaging*, vol. 19, no. 10, pp. 1339–1347, 2001.

[10] F. Liu, B. L. Beck, J. R. Fitzsimmons, S. J. Blackband, and S. Crozier, "A theoretical comparison of two optimization methods for radiofrequency drive schemes in high frequency MRI resonators," *Physics in Medicine and Biology*, vol. 50, pp. 5281–5291, 2005.

[11] W. Mao, M. B. Smith, and C. M. Collins, "Exploring the limits of RF shimming for high-field MRI of the human head," *Magnetic Resonance in Medicine*, vol. 56, no. 4, pp. 918–922, 2006.

[12] P. Ullmann, S. Junge, M. Wick, F. Seifert, W. Ruhm, and J. Hennig, "Experimental analysis of parallel excitation using dedicated coil setups and simultaneous RF transmission on multiple channels," *Magnetic Resonance in Medicine*, vol. 54, no. 4, pp. 994–1001, 2005.

[13] H. Fujita, L. S. Petropoulos, M. A. Morich, S. M. Shvartsmen, and R. W. Brown, "A hybrid inverse approach applied to the design of lumped-element RF coils," *IEEE Transactions on Biomedical Engineering*, vol. 46, no. 3, pp. 353–361, 1999.

[14] H. Fujita, "New horizons in MR technology: RF coil designs and trends," *Magnetic Resonance in Medical Sciences*, vol. 6, no. 1, pp. 29–42, 2007.

[15] C. M. Collins, W. Liu, J. Wang, et al., "Temperature and SAR calculations for a human head within volume and surface coils at 64 and 300 MHz," *Journal of Magnetic Resonance Imaging*, vol. 19, no. 5, pp. 650–656, 2004.

[16] Z. Wang, J. C. Lin, W. Mao, W. Liu, M. B. Smith, and C. M. Collins, "SAR and temperature: simulations and comparison to regulatory limits for MRI," *Journal of Magnetic Resonance Imaging*, vol. 26, no. 2, pp. 437–441, 2007.

[17] J. D. Jackson, *Classical Electrodynamics*, John Wiley & Sons, New York, NY, USA, 3rd edition, 1999.
[18] C. A. Balanis, *Antenna Theory: Analysis and Design*, Harper & Row, New York, NY, USA, 1982.
[19] http://www.fcc.gov/cgi-bin/dielec.sh.
[20] J. Jin, *Electromagnetic Analysis and Design in Magnetic Resonance Imaging*, CRC Press, Boca Raton, Fla, USA, 1999.
[21] C. Wang and G. X. Shen, "B_1 field, SAR, and SNR comparisons for birdcage, TEM, and microstrip coils at 7T," *Journal of Magnetic Resonance Imaging*, vol. 24, no. 2, pp. 439–443, 2006.
[22] K. N. Kurpad and S. M. Wright, "A parallel transmit volume coil with independent control of currents on the array elements," in *Proceedings of the 13th International Society for Magnetic Resonance in Medicine (ISMRM '05)*, p. 16, Miami, Fla, USA, May 2005.